Applied Mathematical Modelling 39 (2015) 483–499

Contents lists available at ScienceDirect

Applied Mathematical Modelling

journal homepage: www.elsevier.com/locate/apm

A validated energy approach for the post-buckling design of micro-fabricated thin film devices

Yasser Safa *, Thomas Hocker

ICP Institute of Computational Physics, ZHAW Zurich University of Applied Sciences, Technikumstrasse 9, CH-8401 Winterthur, Switzerland

ARTICLE INFO

Article history:
Received 19 December 2012
Received in revised form 13 January 2014
Accepted 16 May 2014
Available online 16 June 2014

Keywords:
Buckling
Thin plate
Bifurcation
Energy method
Rayleigh–Ritz

ABSTRACT

The buckling of an elastic thin film is studied in the light of an energy minimization method. Specifically, a comprehensive treatment of the Rayleigh–Ritz method is presented. Detailed mechanical modelling, analytical and numerical derivation of stability criteria, physical interpretation of buckling shapes, numerical code implementation, and experimental validations of selected simulations are addressed.

The thin film deflection is prescribed as a superposition of buckle functions to provide displacement field parameterizations involving trigonometric functions. An energy minimization procedure is applied to calculate the unknown coefficients to predict the buckling shape and amplitude. Critical buckling values representing the thresholds for instability transitions in the system are calculated from the eigenvalues of the Hessian of the potential energy.

Comparison between simulation results and experimental measurements show the great potential of this method to predict thin film buckling. The validated model is exploited by derivation of a new design space for thin film fabrication where the post-buckling mechanics is controlled.

1. Introduction

The highly innovative field of microtechnology provides methods to incorporate mechanical, chemical, fluidic, thermal, optical, or electronic functionality in micro-fabricated structures to allow for compact and efficient product designs. Micro-fabricated devices are used in a wide range of industries, including applications in aerospace, the medical and automotive as well as in robotics and electronics.

In microtechnology, the development of sophisticated membrane mechanics models arose from the need for safe manufacturing and operation of thin film devices prone to different types of mechanical failures.

Although thin plate buckling is usually considered as a failure mode in many macro-scale product design [1], micro-fabricated thin membranes often survive controlled post-buckling stresses as demonstrated, for example, in micro fuel cell applications [2]. Moreover, in stretchable electronics technology, the required regular structures can be generated through the mechanical buckling of thin films [3–5]. Specifically, the periodic wavy shaped membranes in many stretchable components are obtained from controlled heating putting them under in-plane compressive stresses [6]. Therefore the study of thin

* Corresponding author. Tel.: +41 58 934 77 22; fax: +41 58 934 7797.
E-mail address: safa@zhaw.ch (Y. Safa).

http://dx.doi.org/10.1016/j.apm.2014.05.038
0307-904X/

film buckling is a topic of high practical importance. It provides the basis for the reliable design of thin membranes to fulfill the functional requirements even in the buckled state.

When a thin film is deposited at high temperature on a rigid substrate, significant residual stresses usually arise in the film upon cooling. These stresses can be attributed to the extrinsic effects like mismatch thermal expansion between the film and the substrate. For example, compressive stresses arise in the film upon cooling when its thermal expansion coefficient is smaller than that of the substrate. When the compressive stresses are high enough an instability transition takes place and the thin film buckles.

However, buckling can also be driven by inter-granular attraction and repulsion associated with the specifics of thin film deposition [7,8]. Other phenomena that impose intrinsic stresses are phase transformations inside the film, densification, crystallization, and chemical association-dissociation [9].

As example, consider the pulsed laser deposition (PLD) where the deposited film exhibits different stresses depending on the applied deposition conditions. The micro-fabricated fuel cell membranes shown in Fig. 1, for example, exhibits a compressive stresses which cause the membranes to buckle, when deposited at 700 °C. On the other hand, the deposition at room temperature initiates cracks which propagate in the brittle film causing rupture under tensile stresses.

The above example makes clear that the development of appropriate design rules for save manufacturing and operation conditions is highly relevant in thin film technology. Within this context, a major concern in this context is to reduce the number of required experimental data by the use of sophisticated numerical simulations allowing a high fidelity analysis at low experimental costs. In this work, we present a validated model to predict membrane buckling and we show the exploitation range of the implemented numerical method in the development of a design space for thin film manufacturing.

We note from Fig. 1(b) that post-buckling stages of thin films exhibit symmetry breaking shapes of secondary bifurcation and involve complex deformations. Specifically, a secondary buckling shape may exhibit multi-folds including branched sub-folds with wrinkling deformations. Hence, the modelling of such complex buckling behavior and the numerical simulation of the resulting post-buckling shapes are challenging and require advanced computational techniques.

1.1. State of research on thin film buckling

The numerical analysis of thin film buckling has been studied in several research groups by applying different approaches. For example, in [11], Gioia et al. used a membrane energy formulation where the in-plane displacements are constrained to zero and a set of sharp folds i.e. folds with slope discontinuities were obtained. A bending stiffness was added to reproduced yielding smooth folds. The obtained numerical results, as shown by Ortiz in [14], exhibit a good agreement with experimental data with an over estimation of the curvature in the central part of the film. Ortiz also presents a numerical procedure based on shell elements in [14]. Although this method provides a realistic representation of the buckled pattern, it requires a high degree of mesh refinement for an accurate representation of fold wrinkling on the boundaries. Recently, simulation results on thin film buckling were presented by Kerman et al. [12]. They are obtained by using an energy minimization approach of the ridge formation in thin walled structure under compression [13].

Furthermore, important contributions toward a design in post buckling regime were derived by Yamamoto et al. in [2]. However, the application of the employed energy method in [2] is restricted to axis-symmetrical cases describing the first buckling stage. Secondary buckling (i.e. second bifurcation) was not captured and therefore excluded from the design space.

To overcome this limitation, in our work, an energy method based on the Rayleigh–Ritz parameterization is used. Compared to other approaches, it realistically predicts buckling shapes with a low degree of freedom.

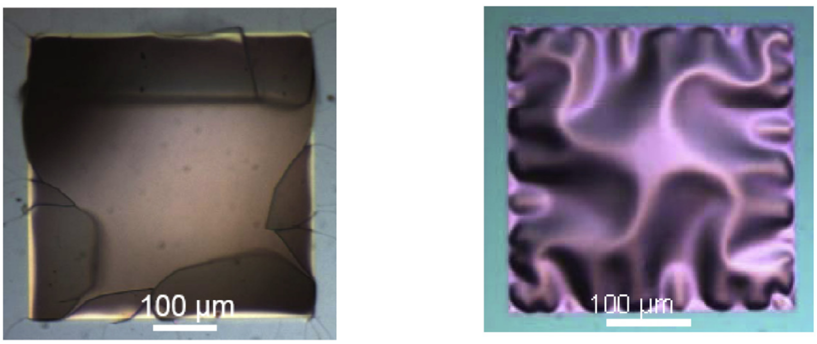

(a) (b)

Fig. 1. Pulsed laser deposition (PLD) of yttria-stabilized zirconia (YSZ) membrane onto a free standing Si_3N_4 layer. Two examples of typical mechanical responses are shown [10]: (a) membrane rupture under residual tensile stresses in YSZ deposited at room temperature, (b) membrane buckling under residual compressive stresses after deposition at 700 °C.

Furthermore, a full exploitation of the energy method is accomplished to provide the informations needed to derive a complete design space for the save fabrication of a deposited thin film. This includes the analysis of mechanical stability, the determination of buckling load and the prediction of primary and secondary modes of post-buckling states. Moreover, we introduce an advanced numerical implementation of the Rayleigh–Ritz method with the aim to predict a realistic representation of the buckling in different stages. The results are validated against experimental measurements and are used to derive a design space for film fabrication. The design concept adopted in this work considers both rupture and buckling and allows a safely use of large area stable films.

2. Modelling of thin film buckling

A stable equilibrium state of the considered mechanical system is ensured by a minimum value of the total potential energy which is assumed to be a restoration energy. Here, the restoration term is attributed to restoring forces (i.e. intermolecular forces) which try to bring the system back to its initial configuration. Under some loading conditions the total potential energy of the system may increase to reach a critical value which corresponds to an unstable state. At this critical value the system may jump to a new configuration by performing a buckling transition to a new stable state.

Specifically, we consider a thin plate model with clamped boundaries where the loading may take the form of a residual in-plane compressive strain. A critical value of this strain induces a sufficiently large potential energy storage to make the compressed film able to perform a buckling transition from the initially flat configuration to an out-of plane deflection.

2.1. Continuum mechanics of the thin film

The strain field in a thin film deposited on a rigid substrate is the result of a combination of different types of deformations. We have the in-plane deformation or membrane strain, which describes the elongation and/or contraction deformation as well as the stretching by shearing deformation of the middle plane of the film. The bending and the twisting deformation of the middle plane represent further contributions to the strain field. Moreover, non-negligible residual strains usually can be found in such thin films due to thermal expansion mismatch, densification and crystallization upon deposition.

When a free standing thin film is mainly exposed to in-plane forces, i.e. out-of-plane tractions are not applied, an in-plane stress based formulation is sufficient. This situation is shown in Fig. 2. To represent the elastic behavior of the thin film with high values of deformation we use the strain tensor ϵ with a nonlinear formulation depending on both the displacement field $\mathbf{u}$ and its gradient $\nabla\mathbf{u}$. Not that in this paper the stress–strain tensors are written in 3D description and then restricted to the 2D case following the in-plane stress simplification:

$$\epsilon = \frac{1}{2}\left[\nabla\mathbf{u}^{\mathbf{T}} + \nabla\mathbf{u} + (\nabla\mathbf{u})^{\mathbf{T}}(\nabla\mathbf{u})\right]. \tag{1}$$

The above relation introduces the classical Green-Saint–Venant (or Green–Lagrange) strain which differs from Cauchy's linear (infinitesimal) strain tensor by the nonlinear quadratic term of the gradient $\nabla\mathbf{u}$. By neglecting the contribution of the in-plane displacement to the quadratic terms, the components of the membrane strain are given by:

$$\epsilon^m_{ij} = \frac{1}{2}\left(\frac{\partial u_i}{\partial j} + \frac{\partial u_j}{\partial i} + \frac{\partial w}{\partial j}\frac{\partial w}{\partial i}\right), \tag{2}$$

with $i, j \in \{x, y\}$ standing for the in-plane coordinates. Here, w denotes the out-of-plane deflection where $\mathbf{u} = (u_x, u_y, w)$. The formulation used in Eq. (2) corresponds to the von Karman plate model.

Isotropic materials are assumed when the residual strain is written in the form of a hydrostatic strain tensor

$$\epsilon^r = \epsilon_0 \mathbb{I}. \tag{3}$$

Here the scalar ϵ_0 represents the average value of the residual strain and $\mathbb{I}$ is the identity (3×3) matrix.

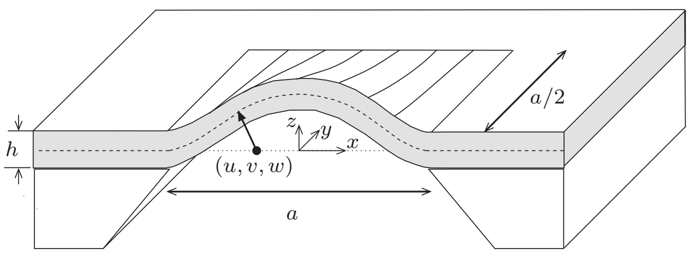

Fig. 2. Schematic representation of the buckling of a thin clamped film with side length a and thickness h. The vector (u, v, w) denotes the displacement of a middle plane point.

The in-plane components of the strain tensor are then given by

$$\epsilon_{ij}(z) = \delta_{ij}\epsilon_0 + \epsilon_{ij}^m + \epsilon_{ij}^b(z), \tag{4}$$

with $\delta_{ij} = (\mathbb{I})_{i,j}$ denoting the Kronecker delta. Note that the bending strain $\epsilon_{ij}^b(z)$ of the film depends on both the curvature and the twist of the middle plane and is given as a linear function of distance z away from the middle plane:

$$\epsilon_{ij}^b(z) = -z\frac{\partial^2 w}{\partial i \partial j}. \tag{5}$$

From Hooke's law we have the following strain–stress relations:

$$\sigma_{ii} = \frac{E}{(1+\nu)(1-2\nu)}(\nu e + (1-2\nu)\epsilon_{ii}),$$
$$\sigma_{ij} = \frac{E}{1+\nu}\epsilon_{ij}.$$

Here, the term e denotes the dilatation $e = \epsilon_{xx} + \epsilon_{yy} + \epsilon_{zz}$ whereas E and ν denote Young's modulus and Poisson's ratio, respectively.

When the out-of-plane stress components are zero, i.e. $\sigma_{xz} = \sigma_{yz} = \sigma_{zz} = 0$, one easily obtains the zero-shear strain components as $\epsilon_{xz} = \epsilon_{yz} = 0$. This leads to Hooke's law for the plane stress situation:

$$\sigma_{xx} = \frac{E}{1-\nu^2}(\epsilon_{xx} + \nu\epsilon_{yy}), \tag{6}$$
$$\sigma_{yy} = \frac{E}{1-\nu^2}(\epsilon_{yy} + \nu\epsilon_{xx}), \tag{7}$$
$$\sigma_{xy} = \frac{E}{1-\nu^2}\epsilon_{xy}. \tag{8}$$

The plate model obtained here deviates from the Kirchhoff plate theory by the fact that the normal out-of-plane strain $\epsilon_{zz} = \frac{-\nu}{1-\nu}(\epsilon_{xx} + \epsilon_{yy})$ is not zero. This is because the normal material lines of the film (i.e. the lines perpendicular to the middle plane) do not satisfy the first Kirchhoff assumption: "The normal material line is infinitely rigid along its own length" (see chapter 16 in [16]).

2.2. The potential energy of the clamped film

We denote by Ω a subset of $\mathbb{R}^3$ representing a thin film of side length a and thickness h as shown in Fig. 2. The total potential energy storage in Ω is expressed as a superposition of various restoration contributions:

$$F = -\int_{\partial\Omega} \sigma \cdot \mathbf{n} \cdot \mathbf{u}\, d\Gamma - \int_{\Omega} \mathbf{f} \cdot \mathbf{u}\, d\Omega + \frac{1}{2}\int_{\Omega} \sigma : \epsilon\, d\Omega.$$

Here, $\mathbf{n}$ is the outward unit normal vector defined on the boundary $\partial\Omega$ and $\mathbf{f}$ is the vector accounting for body forces. The first integral vanishes by considering the clamped boundary conditions:

$$u_x = u_y = w = \frac{\partial w}{\partial n} = 0.$$

The second integral also vanishes by considering the zero body forces. Thus the total potential energy is reduced to the elastic strain energy:

$$F = \frac{1}{2}\int_{\Omega} \sigma : \epsilon\, d\Omega.$$

Using the in-plane Hooke's relations, Eqs. (6)–(8) one gets:

$$F = \frac{E}{2(1-\nu^2)}\int_{-a/2}^{a/2}\int_{-a/2}^{a/2}\int_{-h/2}^{h/2}\left(\epsilon_{xx}^2 + \epsilon_{yy}^2 + 2\nu\epsilon_{xx}\epsilon_{yy} + 2(1-\nu)\epsilon_{xy}^2\right)dx\,dy\,dz.$$

The elastic energy F can be subdivided into the membrane energy F_m and the bending energy F_b:

$$F = F_m + F_b. \tag{9}$$

The membrane energy is associated to the shear as well as elongation or contraction of the middle plane when any bending resistance is excluded. The surface density of the membrane energy is obtained from the integral of the volumic density in z-direction. The total membrane energy is obtained from double integral of the surface energy density:

$$F_m = \frac{Eh}{2(1-\nu^2)}\int_{-a/2}^{a/2}\int_{-a/2}^{a/2}\left(\epsilon_{xx}^2 + \epsilon_{yy}^2 + 2\nu\epsilon_{xx}\epsilon_{yy}\right)_{|z=0} dx\,dy + \frac{Eh}{(1+\nu)}\int_{-a/2}^{a/2}\int_{-a/2}^{a/2}\epsilon_{xy\,|z=0}^2\, dx\,dy. \tag{10}$$

The first integral in Eq. (10) describes the membrane elongation or contraction energy whereas the second integral describes the membrane shear energy.

The bending energy F_b is depending on the curvature and the twist of the film middle plane. The surface density of the bending energy is also obtained from the integral over the vertical "z"-coordinate. When clamped boundary conditions are considered the total bending energy of the domain Ω is given by:

$$F_b = \frac{Eh^3}{24(1-\nu^2)} \int_{-a/2}^{a/2} \int_{-a/2}^{a/2} \left(\frac{\partial^2 w}{\partial x^2} + \frac{\partial^2 w}{\partial y^2} \right)^2 dxdy. \tag{11}$$

According to Eqs. (9)–(11) the membrane stiffness is of order $O(h)$ whereas the bending stiffness is order $O(h^3)$. This implies that for an extremely thin plate ($h \longrightarrow 0$) under a given compressive-bending loading, the bending energy storage results in a high degree of twist-curvature deformation.

2.3. Reduced variables

The model as introduced in the above equations contains a rather large number of variables, parameters and coefficients. However, the buckling solution, depends only on certain combinations of these terms and not necessarily on each one separately. In order to simplify the formulation let us to introduce the following reduced quantities:

- coordinates: $\overline{x} = \frac{x}{a}$, $\overline{y} = \frac{y}{a}$, $\overline{z} = \frac{z}{h}$,
- displacements: $\overline{u} = \frac{u_x a}{h^2}$, $\overline{v} = \frac{u_y a}{h^2}$, $\overline{w} = \frac{w}{h}$,
- energy: $\overline{F} = \frac{F(1-\nu^2)a^2}{Eh^5}$.

The bending energy in reduced form is denoted by $\overline{F}_b$ and given as

$$\overline{F}_b = \frac{1}{12} \int_{-1/2}^{1/2} \int_{-1/2}^{1/2} \left(\frac{\partial^2 \overline{w}}{\partial \overline{x}^2} \right)^2 + \frac{\partial^2 \overline{w}}{\partial \overline{x}^2} \frac{\partial^2 \overline{w}}{\partial \overline{y}^2} \, d\overline{x} d\overline{y}. \tag{12}$$

The reduced membrane energy $\overline{F}_m$ is a summation of two energetic contributions: firstly, the shear energy i $\overline{F}_s$, given as

$$\overline{F}_s = \frac{1}{2} \int_{-1/2}^{1/2} \int_{-1/2}^{1/2} (1-\nu) \left(\frac{\partial \overline{u}}{\partial \overline{y}} \frac{\partial \overline{v}}{\partial \overline{x}} + 2 \frac{\partial \overline{u}}{\partial \overline{y}} \frac{\partial \overline{w}}{\partial \overline{x}} \frac{\partial \overline{w}}{\partial \overline{y}} + 1/2 \left(\frac{\partial \overline{w}}{\partial \overline{x}} \frac{\partial \overline{w}}{\partial \overline{y}} \right)^2 \right) d\overline{x} \, d\overline{y}, \tag{13}$$

and secondly, the elongation or contraction energy $\overline{F}_e$, given as

$$\begin{aligned} \overline{F}_e = \frac{1}{2} \int_{-1/2}^{1/2} \int_{-1/2}^{1/2} & (1+\nu)\overline{\epsilon_0}^2 + 2\left(\frac{\partial \overline{u}}{\partial \overline{x}} \right)^2 + (1-\nu)\left(\frac{\partial \overline{u}}{\partial \overline{y}} \right)^2 + 2\nu \frac{\partial \overline{u}}{\partial \overline{x}} \frac{\partial \overline{v}}{\partial \overline{y}} + 2 \frac{\partial \overline{u}}{\partial \overline{x}} \left(\frac{\partial \overline{w}}{\partial \overline{x}} \right)^2 + 2\nu \frac{\partial \overline{u}}{\partial \overline{x}} \left(\frac{\partial \overline{w}}{\partial \overline{y}} \right)^2 \\ & + 2\overline{\epsilon_0}(1+\nu)\left(\frac{\partial \overline{w}}{\partial \overline{x}} \right)^2 + 1/2 \left(\frac{\partial \overline{w}}{\partial \overline{x}} \right)^4 + 1/2 \left(\frac{\partial \overline{w}}{\partial \overline{x}} \frac{\partial \overline{w}}{\partial \overline{y}} \right)^2 d\overline{x} \, d\overline{y}. \end{aligned} \tag{14}$$

Here the term $\overline{\epsilon_0} = \frac{a^2}{h^2} \epsilon_0$ denotes the reduced value of the residual strain in the film, given in Eq. (3). Note that the above expression has been simplified since terms like $\left(\frac{\partial \overline{u}}{\partial \overline{x}}\right)^2$ and $\left(\frac{\partial \overline{v}}{\partial \overline{y}}\right)^2$ yield the some values upon integration. Similarly, the integral of the terms $\frac{\partial \overline{u}}{\partial \overline{x}} \left(\frac{\partial \overline{w}}{\partial \overline{y}}\right)^2$ and $\frac{\partial \overline{v}}{\partial \overline{y}} \left(\frac{\partial \overline{w}}{\partial \overline{x}}\right)^2$ yield the some values.

The quadratic terms in Eqs. (12)–(14) correspond to the elastic energy when Cauchy's linear (infinitesimal) strain model is applied. Note that it is a feature of the employed energy method, the higher order terms in Eqs. (13) and (14) introduce a nonlinear energy correction that allows one to predict the post-buckling shape, amplitude and stability. On the contrary, a linear eigenvalue analysis would only provide values for the buckling load and shape but no information about post-buckling amplitude.

3. Energy method

Analysis of thin film buckling at the prediction of the various buckling stages and the corresponding buckling loads and amplitudes.

The shape of the buckled film is indicative of the buckling stage: we distinguish between two modal states corresponding to two ranges of in-plane loading values in the flat film, see Fig. 3(a). The first one is the primary buckling mode which is characterized by an axis-symmetric shape, see Fig. 3(b). It takes place when the in-plane compression in the flat film reaches the buckling load. The second state is the secondary buckling which is produced by a higher range of in-plane loading values. We recall that secondary buckling is characterized by the axis-symmetry breaking though maintaining a rotationally symmetric shape C_4^z ($\frac{2\Pi}{4}$ around z-axis), see Fig. 3(c). To proceed further, a parameterization method is applied to represent the displacement fields and then a numerical minimization procedure is used to determine the corresponding buckling amplitude.

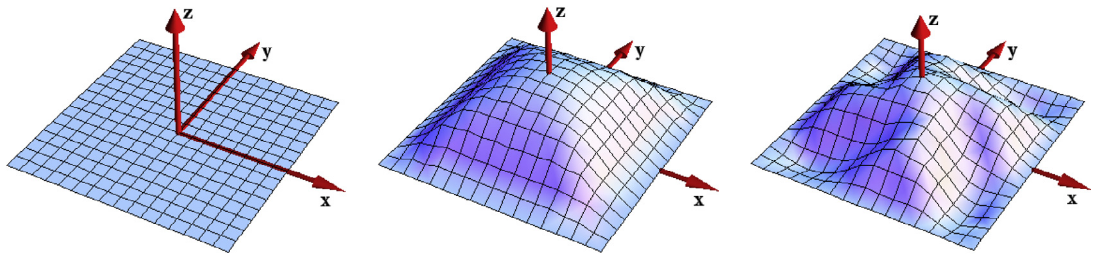

(a) (b) (c)

Fig. 3. Film schematic: (a): Unbuckled. (b): Primary buckling. (c): Secondary buckling.

3.1. Rayleigh–Ritz parameterization

In the framework of the Rayleigh–Ritz method, see [17], the displacement fields are represented as a sum of double trigonometric trial functions. Those functions need to be differentiable to represent the strain term in the energy integral. They should also satisfy "at least" the essential (Dirichlet) boundary conditions. To proceed further, the in-plane displacement along x-direction is formulated as a double Fourier series expansion of order p:

$$\overline{u}(\overline{x},\overline{y}) = \sum_{i,j=1}^{p} u^s_{ij} f_{ij}(\overline{x},\overline{y}) + \sum_{i,j=1}^{p} u^a_{ij} f_{ij}(\overline{y},\overline{x}). \tag{15}$$

Here f_{ij} is the set of trial functions which satisfy the conditions of the fixed boundaries

$$f_{ij}(\overline{x},\overline{y}) = sin(2i\pi\overline{x})\, cos((2j-1)\pi\overline{y}). \tag{16}$$

The functions $f_{ij}(\overline{x},\overline{y})$ satisfy the mirror symmetric mode (reflection symmetry) with respect to the oyz-plane, with unknown coefficients u^s_{ij}, see Fig. 3(b). Likewise, the trial functions $f_{ij}(\overline{y},\overline{x})$ satisfy the anti-mirror symmetric mode with unknown coefficients u^a_{ij}, see Fig. 3(c).

With this formalism the rotationally symmetric shape C^z_4 ($\frac{2\Pi}{4}$ around z-axis) of the in-plane displacements is ensured by formulating the displacement along y-direction as

$$\overline{v}(\overline{x},\overline{y}) = \overline{u}(\overline{y},-\overline{x}). \tag{17}$$

Furthermore, the out-of-plane deflection is parameterized as a sum of buckle functions

$$\overline{w}(\overline{x},\overline{y}) = \sum_{i=1,j=i}^{m} w^s_{ij} g^s_{ij}(\overline{x},\overline{y}) + \sum_{i=1,j=i+1}^{m} w^a_{ij} g^a_{ij}(\overline{x},\overline{y}), \tag{18}$$

where the trial functions g^s_{ij} satisfy the mirror symmetry with respect to the oxz- and oyz- planes:

$$g^s_{ij}(\overline{x},\overline{y}) = \left(cos(2i\pi\overline{x}) - (-1)^i\right)\left(cos(2j\pi\overline{y}) - (-1)^j\right) + \left(cos(2j\pi\overline{x}) - (-1)^j\right)\left(cos(2i\pi\overline{y}) - (-1)^i\right). \tag{19}$$

The functions g^a_{ij} satisfy the anti-mirror symmetry with respect to the oxz- and oyz- planes:

$$\begin{aligned} g^a_{ij}(\overline{x},\overline{y}) = &\left(sin((2i+1)\pi\overline{x}) - (-1)^i sin(\pi\overline{x})\right)\left(sin((2j+1)\pi\overline{y}) - (-1)^j sin(\pi\overline{y})\right) \\ &- \left(sin((2j+1)\pi\overline{x}) - (-1)^j sin(\pi\overline{x})\right)\left(sin((2i+1)\pi\overline{y}) - (-1)^i sin(\pi\overline{y})\right). \end{aligned} \tag{20}$$

Both g^s_{ij} and g^a_{ij} satisfy the rotational symmetry C^z_4. At the boundaries $\overline{x} = \pm 1/2$ and $\overline{y} = \pm 1/2$, the natural conditions of clamped edges are satisfied through the derivatives $\frac{\partial g^s_{ij}}{\partial \overline{x}} = \frac{\partial g^s_{ij}}{\partial \overline{y}} = \frac{\partial g^a_{ij}}{\partial \overline{x}} = \frac{\partial g^a_{ij}}{\partial \overline{y}} = 0$, where the essential boundary conditions are ensured by $f_{ij} = g^s_{ij} = g^a_{ij} = 0$. Buckling shape and amplitude are determined from the values of the coefficients w^s_{ij} and w^a_{ij} which are obtainable by applying a minimization procedure i.e. the conjugate gradient method. Note that the Rayleigh–Ritz approach is a mesh free method. Therefore the degree of freedom of the problem depends only on the degree of Ritz expansion in Eqs. (15) and (18) where the total number of unknowns is $m^2 + 2p^2$.

4. Derivation of criteria for the instability transition

The displacement amplitudes can be expressed as a tensor field. In this work a vector representation of amplitudes has been chosen to perform the stability analysis. The set of in-plane amplitude terms $\{u^s_{ij}\}^p_{i,j=1} \cup \{u^a_{ij}\}^p_{i,j=1}$ is introduced by the vector $\vec{U} \in \mathbb{R}^{2p^2}$. We "abuse" notation by writing $\vec{U}$ as a one-column matrix in $\mathcal{M}_{2p^2,1}(\mathbb{R})$:

$$\left(u^s_{1\,1} \quad \cdots \quad u^s_{1\,p} \quad u^s_{2\,1} \quad \cdots \quad \cdots \quad u^s_{p\,p} \quad u^a_{1\,1} \quad \cdots \quad u^a_{1\,p} \quad u^a_{2\,1} \quad \cdots \quad \cdots \quad u^a_{p\,p} \right)^T, \tag{21}$$

where the superscript ^{T} denotes the transpose. The set of out-of-plane amplitudes $\{w^s_{ij}\}^m_{i=1,j=i} \cup \{w^a_{ij}\}^m_{i=1,j=i+1}$ is represented in a similar way. Furthermore we introduce the vector $\vec{W} \in \mathbb{R}^{m^2}$ as

$$\left(w^s_{1\,1} \quad \cdots \quad w^s_{1\,m} \quad w^s_{2\,2} \quad \cdots \quad \cdots \quad w^s_{m\,m} \quad w^a_{1\,2} \quad \cdots \quad w^a_{1\,m} \quad w^a_{2\,3} \quad \cdots \quad \cdots \quad w^a_{m-1\,m} \right)^T. \tag{22}$$

The analysis in the remaining parts deals with the amplitude vectors $\vec{U}, \vec{W}$, as well as the reduced residual strain $\overline{\epsilon}_0$.

4.1. The energy formulation for a stationary state

The total potential energy is reintroduced here in reduced form as a differentiable function

$$\begin{aligned} &\overline{F} : \mathbb{R}^{2p^2} \times \mathbb{R}^{m^2} \times \mathbb{R} \longrightarrow \mathbb{R} \\ &(\vec{U},\ \vec{W},\ \overline{\epsilon}_0) \longrightarrow \overline{F}(\vec{U},\ \vec{W},\ \overline{\epsilon}_0). \end{aligned} \tag{23}$$

Based on Eqs. (12)–(14), the function $\overline{F}$ is quadratic in $\vec{U}$ and quartic in $\vec{W}$.

At an equilibrium state the minimum potential energy implies the in-plane stationary condition:

$$\partial_{\vec{U}} \overline{F} \ = \ \vec{0}.$$

Note that the in-plane partial derivative $\partial_{\vec{U}}$ is represented by $\left(\frac{\partial}{\partial U_1}\ \frac{\partial}{\partial U_2} \cdots \frac{\partial}{\partial U_{p^2}} \cdots \frac{\partial}{\partial U_{2p^2}} \right)^T$. This condition yields the nonlinear system of equations given by

$$A.\vec{U} - \vec{V}(\vec{W}) \ = \ \vec{0}. \tag{24}$$

Here A is a definite positive symmetric real matrix (and thus invertible) of order $2p^2$ i.e. $\in \mathcal{M}_{2p^2,2p^2}(\mathbb{R})$ and the vector $\vec{V} \in \mathbb{R}^{2p^2}$ is a quadratic function of $\vec{W}$. The in-plane displacement vector is obtained as a quadratic function of the vector $\vec{W}$:

$$\vec{U} \ = \ \vec{G}(\vec{W}) \ = \ A^{-1}\vec{V}(\vec{W}). \tag{25}$$

Now the energy is readily obtained as an explicit quartic function of the out-of-plane displacement

$$\overline{F} \ = \ \overline{F}\Big(\vec{G}(\vec{W}),\ \vec{W},\ \overline{\epsilon}_0\Big). \tag{26}$$

For a given reduced residual strain $\overline{\epsilon}_0$ the energy in a stable equilibrium state is estimated through the vector $\vec{W}_{eq}$ which satisfies the condition:

$$\overline{F}_{min} = \overline{F}\Big(\vec{G}(\vec{W}_{eq}),\ \vec{W}_{eq},\ \overline{\epsilon}_0\Big) = \min_{\vec{W} \in \mathbb{R}^{m^2}} \overline{F}\Big(\vec{G}(\vec{W}),\ \vec{W},\ \overline{\epsilon}_0\Big). \tag{27}$$

In this reduced formulation, $\overline{F}_{min}$ depends only on v and on $\overline{\epsilon}_0$. An out-of-plane stationary condition is necessarily satisfied at the local minimum point $(\vec{W} = \vec{W}_{eq}, \overline{\epsilon}_0)$ of $\overline{F}$:

$$D_{\vec{W}} \overline{F}(\vec{U},\ \vec{W},\ \overline{\epsilon}_0)_{\substack{\vec{U}=\vec{G}(\vec{W}) \\ \vec{W}=\vec{W}_{eq}}} = 0, \tag{28}$$

where $D_{\vec{W}}$ is the first derivative with respect to $\vec{W}$, defined as

$$D_{\vec{W}} = (\partial_{\vec{W}}\vec{U}) \ \cdot \ \partial_{\vec{U}} + \ \partial_{\vec{W}},$$

with

$$(\partial_{\vec{W}}\vec{U}) = \partial_{\vec{W}}\ \vec{U}^T \quad \text{and} \quad \partial_{\vec{W}} = \left(\frac{\partial}{\partial W_1}\, \frac{\partial}{\partial W_2} \cdots \frac{\partial}{\partial W_{m^2}} \right)^T.$$

Although the aforementioned stationarity is a necessary condition for the stable equilibrium state it may also correspond to an unstable saddle point. In the following sections, we will see that the double derivatives of the energy function with respect to the displacements result in a Hessian matrix with eigenvalues depending on the system's stability.

4.1.1. The Hessian formulation

We start by introducing the double derivative operator

$$D_{\vec{W},\vec{W}} \ = \ D_{\vec{W}}\ [D_{\vec{W}}].$$

Furthermore, the energy function in Eq. (23) is assumed to be smooth with second order derivative. In the stationary state the first in-plane derivative satisfies $\partial_{\vec{U}}\overline{F} = \vec{0}$, hence one has $\vec{U} = \vec{G}(\vec{W})$ (see Eq. (25)) and the double derivative of the energy function $\overline{F}$ becomes

$$\Big[D_{\vec{W},\vec{W}}\overline{F}\Big]_{\vec{U}=\vec{G}(\vec{W})} = \Big[\partial_{\vec{W}}\vec{U}\ \partial_{\vec{U}}\partial_{\vec{U}}\overline{F}\ (\partial_{\vec{W}}\vec{U})^T \ + \ \partial_{\vec{W}}\vec{U}\ \partial_{\vec{U}}\partial_{\vec{W}}\overline{F} + \partial_{\vec{W}}\partial_{\vec{U}}\overline{F}\ (\partial_{\vec{W}}\vec{U})^T \ + \ \partial_{\vec{W}}\partial_{\vec{W}}\overline{F}\Big]_{\vec{U}=\vec{G}(\vec{W})}.$$

Note that $\left(\partial_{\vec{U}}\partial_{\vec{W}}\overline{F}\right)^T = \partial_{\vec{W}}\partial_{\vec{U}}\overline{F} = -\partial_{\vec{W}}\vec{V}$. Within an equilibrium state at the point $(\overline{\epsilon}_0, \vec{W}_{eq})$, the relation $\vec{U} = A^{-1}\vec{V}$ is satisfied and the Hessian at this point is obtained as

$$\mathcal{H}(\overline{\epsilon}_0, \vec{W}_{eq}) = \left[D_{\vec{W},\vec{W}}\overline{F}\right]_{\substack{\vec{U}=\vec{G}(\vec{W})\\ \vec{W}=\vec{W}_{eq}}} = \left[-\partial_{\vec{W}}\vec{V}A^{-1}\left(\partial_{\vec{W}}\vec{V}\right)^T + \partial_{\vec{W}}\partial_{\vec{W}}\overline{F}\right]_{\substack{\vec{U}=\vec{G}(\vec{W})\\ \vec{W}=\vec{W}_{eq}}}, \tag{29}$$

which is a symmetric real matrix (thus it is orthogonally diagonalizable) of order m^2 i.e. $\in \mathcal{M}_{m^2,m^2}(\mathbb{R})$.

In the pre-buckling equilibrium stage where the film has a flat shape, the out-of-plane deflection amplitudes are zeros i.e. $\vec{W} = \vec{0}$. Hence the derivative $\partial_{\vec{W}}\vec{V}$ vanishes since $\vec{V}$ is a quadratic function of $\vec{W}$ and hence the Hessian in the pre-buckling equilibrium state is obtained by the simplified expression:

$$\mathcal{H}(\overline{\epsilon}_0, \vec{0}) = \left[\partial_{\vec{W}}\partial_{\vec{W}}\overline{F}\right]_{\substack{\vec{U}=\vec{G}(\vec{W})\\ \vec{W}=\vec{0}}}. \tag{30}$$

4.2. Prediction of primary buckling

In simple terms, the buckling load is the physical threshold at which the equilibrium state of the structure suddenly changes from stable to unstable [18].

We proceed by a stability analysis of the system to derive the critical value for the instability transition. We consider the system in equilibrium at the point $(\overline{\epsilon}_0, \vec{W}_{eq})$. The second order expansion around $\vec{W}_{eq}$ is then given by

$$\overline{F}\left(\vec{G}(\vec{W}_{eq} + \delta\vec{W}),\ \vec{W}_{eq} + \delta\vec{W},\ \overline{\epsilon}_0\right) \approx \overline{F}\left(\vec{G}(\vec{W}_{eq}),\ \vec{W}_{eq},\ \overline{\epsilon}_0\right) + \delta\vec{W}^T \cdot \left[D_{\vec{W}}\overline{F}\right]_{\substack{\vec{U}=\vec{G}(\vec{W})\\ \vec{W}=\vec{W}_{eq}}} + \frac{1}{2}\delta\vec{W}^T \cdot \left[D_{\vec{W},\vec{W}}\overline{F}\right]_{\substack{\vec{U}=\vec{G}(\vec{W})\\ \vec{W}=\vec{W}_{eq}}}\delta\vec{W}, \tag{31}$$

where $\delta\vec{W}$ is a perturbation of "small" amplitude. At the equilibrium point $(\overline{\epsilon}_0, \vec{W}_{eq})$ we then get

$$\left[D_{\vec{W}}\overline{F}\right]_{\substack{\vec{U}=\vec{G}(\vec{W})\\ \vec{W}=\vec{W}_{eq}}} = \vec{0} \quad \text{and} \quad \left[D_{\vec{W},\vec{W}}\overline{F}\right]_{\substack{\vec{U}=\vec{G}(\vec{W})\\ \vec{W}=\vec{W}_{eq}}} = \mathcal{H}(\overline{\epsilon}_0, \vec{W}_{eq}).$$

Furthermore, the energy variant $\delta\overline{F}$ induced by the perturbation $\delta\vec{W}$ at this point is written as

$$\delta\overline{F} = \frac{1}{2}\delta\vec{W}^T \cdot \mathcal{H}(\overline{\epsilon}_0, \vec{W}_{eq})\,\delta\vec{W}. \tag{32}$$

The equilibrium state $(\overline{\epsilon}_0, \vec{W}_{eq})$ is a stable point of the mechanical system if, for any perturbation $\delta\vec{W}$, the energy variant is strictly positive, i.e. $\delta\overline{F} > 0$. In contrast, $(\overline{\epsilon}_0, \vec{W}_{eq})$ is an instability point if, for the same value of $\overline{\epsilon}_0 = \overline{\epsilon}_0^c < 0$, there is a perturbation $\delta\vec{W}$ for which the system preserves the same energy. I.e. we have an energy invariant $\delta\overline{F} = 0$ written as

$$\frac{1}{2}\delta\vec{W}^T \cdot \mathcal{H}(\overline{\epsilon}_0, \vec{W}_{eq})\,\delta\vec{W} = 0. \tag{33}$$

Eq. (33) holds with a non trivial solution $(\delta\vec{W} \neq \vec{0})$ if, and only if, for a critical value $\overline{\epsilon}_0 = \overline{\epsilon}_0^c$ the matrix $\mathcal{H}$ is singular i.e. $Det\,\mathcal{H} = 0$. Consequently, at this unstable equilibrium point $(\overline{\epsilon}_0^c, \vec{W}_{eq})$, the singular matrix $\mathcal{H}$ has a zero eigenvalue $\lambda^c = 0$ and the energy variant induced by the perturbation $\delta\vec{W}_{ev}$ in the direction of the λ^c-eigenvector $\vec{W}_{ev}$ is given by

$$\delta\overline{F} = \frac{1}{2}\delta\vec{W}_{ev}^T \cdot \mathcal{H}(\overline{\epsilon}_0^c, \vec{W}_{eq})\delta\vec{W}_{ev} = \frac{\lambda^c}{2}\|\delta\vec{W}_{ev}\|^2 = 0. \tag{34}$$

Within this unstable stationary state, an external traction in the direction of $\vec{W}_{ev}$ drives the system to perform a transition toward an equilibrium stable state. A mathematical interpretation of the aforementioned instability is the loss of the "strong convex" property of the energy function $\overline{F}$ at the point $(\overline{\epsilon}_0^c, \vec{W}_{eq})$ in the direction of $\vec{W}_{ev}$ where the approximative curvature κ of $\overline{F}$ is estimated as

$$\kappa = \frac{\vec{W}_{ev}^T \cdot \mathcal{H}(\overline{\epsilon}_0, \vec{W}_{eq})\,\vec{W}_{ev}}{\|\vec{W}_{ev}\|^2} = \lambda^c = 0. \tag{35}$$

Now we restrict the analysis to the unbuckled film state by considering the equilibrium path (fundamental path of the trivial solution $\vec{W}_{eq} = \vec{0}$, denoted as FP1 in Fig. 4). The onset of the first unstable equilibrium (primary buckling) is attributed to a threshold value of reduced compressive strain $\overline{\epsilon}_0 = \overline{\epsilon}_0^{c_1} < 0$ (buckling load) when the minimum eigenvalue of $\mathcal{H}(\overline{\epsilon}_0^{c_1}, \vec{0})$ denoted by $\lambda^{c_1} = \lambda_{min} = \min\{\lambda_i\}_{i=1}^{m^2}$ vanishes. For $\overline{\epsilon}_0 < \overline{\epsilon}_0^{c_1}$ the equilibrium path of zero-deflection, noted as FP2 in Fig. 4, cannot be a stable state for the system and therefore a stable equilibrium point $(\overline{\epsilon}_0, \vec{W}_{eq})$ should belong to the primary buckling path denoted as BP1.

4.3. Interpretation and prediction of secondary buckling

Within a range of high in-plane compressive values where $\overline{\epsilon}_0 < \overline{\epsilon}_0^{c_1}$, there is a reduced residual strain value $\overline{\epsilon}_0^{c_2} < 0$ for which the Hessian matrix $\mathcal{H}$ at the equilibrium point $(\overline{\epsilon}_0^{c_2}, \vec{W}_{eq} = 0)$ has a multiple eigenvalue $\lambda^{c_2} = 0$. At this point there

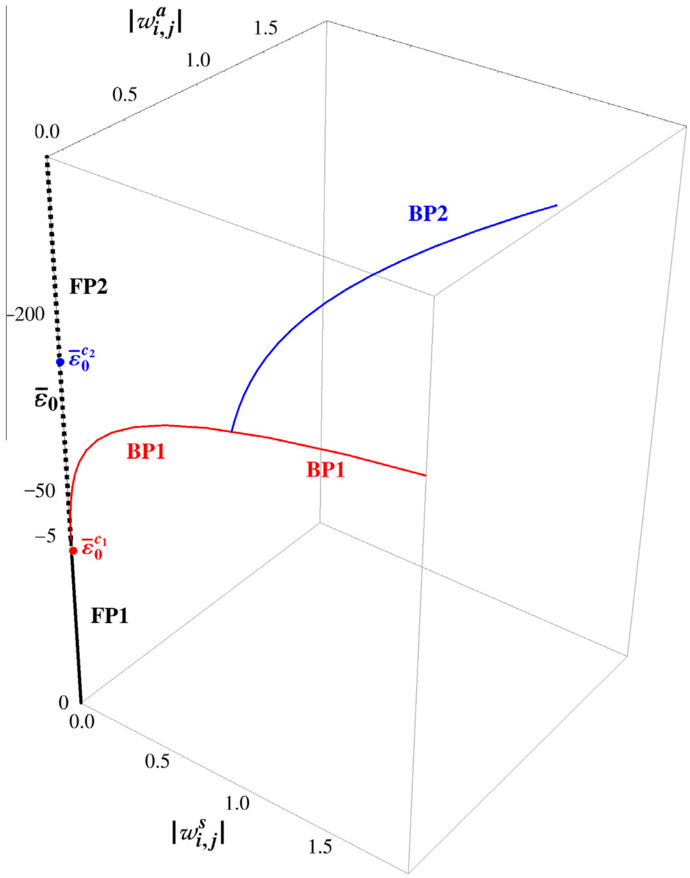

Fig. 4. Schematic of the bifurcation of the equilibrium solution $(\bar{\epsilon}_0, \vec{W}_{eq})$. FP1: fundamental path of a stable unbuckled state $(\bar{\epsilon}_0 > \bar{\epsilon}_0^{c_1}, \vec{W}_{eq} = \vec{0})$. FP2: fundamental path of an unstable unbuckled state $(\bar{\epsilon}_0 < \bar{\epsilon}_0^{c_1}, \vec{W}_{eq} = \vec{0})$. BP1: primary bifurcation path with axis symmetry shape $(\bar{\epsilon}_0 < \bar{\epsilon}_0^{c_1}, | w^s_{i,j} | > 0, w^a_{i,j} = 0)$. BP2: secondary bifurcation path with symmetry breaking shape $(\bar{\epsilon}_0 < \bar{\epsilon}_0^{c_1}, | w^s_{i,j} | > 0, | w^a_{i,j} | > 0)$.

are two orthogonal λ^{c_2}-eigenvectors of $\mathcal{H}$: a symmetric mode vector $\vec{W}^s_{ev}$ and an asymmetric mode vector $\vec{W}^a_{ev}$. The response of the system to the perturbations $\delta\vec{W}^s_{ev}$ and $\delta\vec{W}^a_{ev}$ of "small" amplitude in the direction of the λ^{c_2}-eigenvectors is expressed by an energy invariant estimated similarly to Eq. (34):

$$\delta\bar{F} = \frac{\lambda^{c_2}}{2}\|\delta\vec{W}^s_{ev}\|^2 = \frac{\lambda^{c_2}}{2}\|\delta\vec{W}^a_{ev}\|^2 = 0. \tag{36}$$

Therefore the system has multiple directions of instability for $\bar{\epsilon}_0 = \bar{\epsilon}_0^{c_2}$. Note that double buckling point has been reported in several cases, see e.g. [19], and is associated with an eigenvalue multiplicity. Beyond this critical value, where $\bar{\epsilon}_0 < \bar{\epsilon}_0^{c_2}$, the film may buckle either into the path of primary buckling with symmetric mode or into the path of secondary buckling with symmetry-breaking mode denoted as BP2 in Fig. 4.

We suggest the following numerical procedure to investigate the second bifurcation:

- Starting step $(\bar{\epsilon}_0, \vec{W}) \in$ BP2. (see Fig. 4)
- do while $D > 0$
- Set: $\bar{\epsilon}_0 = \bar{\epsilon}_0 + | \Delta\bar{\epsilon}_0 |$ (decrement residual compression)
- Find $\vec{W}_{eq}$ such that $\bar{F}\left(\vec{G}(\vec{W}_{eq}), \vec{W}_{eq}, \bar{\epsilon}_0\right) = \min_{\vec{W}\in\mathbb{R}^{m^2}} \bar{F}\left(\vec{G}(\vec{W}), \vec{W}, \bar{\epsilon}_0\right)$ (see Eq. (27)
- Set: $D = Det\,\mathcal{H}(\bar{\epsilon}_0, \vec{W}_{eq})$ (see Eq. (29)
- enddo
- Set: $\bar{\epsilon}_0^{c_2} = \bar{\epsilon}_0$

Starting from a breaking symmetry mode, we apply the energy minimization in order to locate an equilibrium solution $(\bar{\epsilon}_0, \vec{W}_{eq})$ which belongs to the secondary path BP2 in Fig. 4. We proceed with an iterative incrementation of $\bar{\epsilon}_0$. At each step, we perform an energy minimization initialized from the current solution and a new equilibrium point is then located on BP2. The minimum eigenvalue ($\lambda_{min} \geqslant 0$) of the Hessian matrix (see Eq. (29)) is evaluated at each step until the stop condition

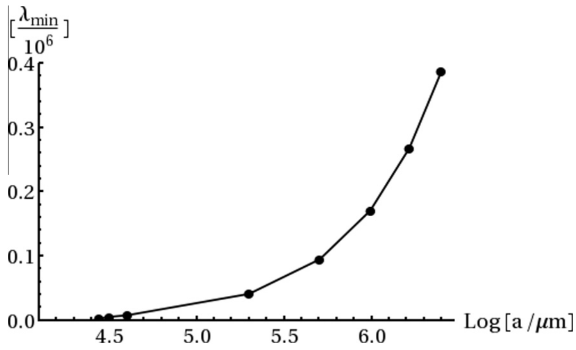

Fig. 5. The degree of stability of secondary buckling at $\epsilon_0 = -0.002$ represented by the minimum eigenvalues of the Hessian on the secondary post-buckling path.

$\lambda_{min}(\overline{\epsilon}_0) = 0$ is satisfied for $\overline{\epsilon}_0 = \overline{\epsilon}_0^{c_2}$. This indicates that secondary buckling cannot be a stable post buckling state below a threshold $|\overline{\epsilon}_0^{c_2}|$ (i.e. for $\overline{\epsilon}_0 > \overline{\epsilon}_0^{c_2}$) where the stable equilibrium point $(\overline{\epsilon}_0, \vec{W}_{eq})$ should belong to the primary buckling path noted by BP1 in Fig. 4.

Fig. 5 shows the variation of the minimum eigenvalue of the Hessian in the secondary buckling path as function of the side length of the square film. For a given compressive strain of $\epsilon_0 = -0.002$ and a film thickness of h = 300 nm the reduced strain is a function of the side length a, i.e. $\overline{\epsilon}_0 = \frac{a^2}{h^2}\epsilon_0$. The secondary buckling starts when the side length a is equal to 85 μm which corresponds to $\overline{\epsilon}_0^{c_2} = -161 \approx 42\ \overline{\epsilon}_0^{c_1}$ where $\overline{\epsilon}_0^{c_1} = -3.63$. The accuracy of this estimation depends on the expansion degree. Here we have used $m = 3$ and $p = 6$.

5. Numerical implementation and experimental validation

The above described energy method to predict the buckling behavior of thin films has been implemented in *Mathematica*. The code includes the Rayleigh–Ritz parameterization, the first and the second derivatives of the displacement, and a numerical integration over the square geometry of the film using the quadrature technique. The integral of the energy terms satisfying the rotational C_4^z property is estimated by the numerical integration over the corner square $[0, 0.5]^2$ up to factor 4.

The implementation of the out-of-plane amplitudes as a nonlinear function of the in-plane amplitudes in Eq. (25) was also simplified based on the symmetric and asymmetric properties of the trial functions. The minimization procedure is applied by using the conjugate gradient method (already available in *Mathematica*) to determine the coefficients of the out-of-plane amplitude (see Eq. (18)). Furthermore, a post-processing *Mathematica* routine was implemented to calculate the in-plane displacements, stresses, strain, and yielding fields.

The stability conditions of pre-buckling as well as the first and second post-buckling stages are investigated according to the eigenvalues of an implemented *Mathematica* Hessian matrix of the double derivatives of the energy (see Eq. (29)).

As already mentioned this method is mesh free with $2p^2 + m^2$ unknowns. The use of in-plane equilibrium conditions reduces the degree of freedom of the problem to m^2. Regarding the shape of trigonometric formulation of the trial functions in Eqs. (16), (19) and (20), an accurate numerical integration was ensured by using at least 100 $\max\{m^2, p^2\}$ quadrature points.

5.1. Implementation tests and validations

A symmetry test of the implemented code has been successfully passed by comparing the numerical values of the energy in each corner representing a quarter of the film domain $[-0.5, 0.5]^2$. The implementation of the stiffness matrix A in Eq. (25) was examined by comparing the energy norm of the in-plane displacement $||\vec{U}||_A = \frac{1}{2}\vec{U}^T \cdot A\vec{U}$ with the numerical integration of the membrane energy related to a linear model and expressed by the quadratic terms in Eqs. (13) and (14).

A *Mathematica* routine based on the finite difference method has been implemented to calculate the double derivative of the energy at the equilibrium point $(\overline{\epsilon}_0, \vec{W}_{eq})$ where $\vec{U} = \vec{G}(\vec{W})$ is satisfied:

$$\vec{e}_i \cdot \mathcal{H}(\overline{\epsilon}_0, \vec{W}_{eq})\vec{e}_i \approx \frac{\overline{F}_{|\vec{W}=\vec{W}_{eq}+\varepsilon\vec{e}_i} + \overline{F}_{|\vec{W}=\vec{W}_{eq}-\varepsilon\vec{e}_i} - 2\overline{F}_{|\vec{W}=\vec{W}_{eq}}}{\varepsilon^2}. \tag{37}$$

Here $\{\vec{e}_i\}_{i=1}^{m^2}$ is a set of normalized vectors spanning the space $\mathbb{R}^{m^2}$ and the scalar ε denotes the magnitude of a "small" step of centered discretization applied around $(\overline{\epsilon}_0, \vec{W}_{eq})$ in the direction of $\vec{e}_i$.

The implementation of the Hessian matrix, Eq. (29), is validated by comparing its diagonal terms to the values obtained by the finite difference in Eq. (37) by substituting for $\{\vec{e}_i\}_{i=1}^{m^2}$ the canonical basis of $\mathbb{R}^{m^2}$. The Hessian matrix is also validated by comparing its eigenvalues to those obtained by Eq. (37) by substituting for $\{\vec{e}_i\}_{i=1}^{m^2}$ a set of the corresponding normalized eigenvectors.

Table 1
Prediction of the threshold value of the residual compressive strain $\bar{\epsilon}_0^{c_2}$ for the secondary buckling at the second bifurcation point.

Poisson ratio ν	Finite elements: $\bar{\epsilon}_0^{c_2}$	This work: $\bar{\epsilon}_0^{c_2}$
0.00	−226.0	−225.2
0.15	−211.9	−213.4
0.25	−206.0	−207.6
Discretization/expansion degree	6000 Shell elements	66 Parameters

Note that the first buckling load resulting from the zero eigenvalue of the pre-buckling Hessian has the value of $\bar{\epsilon}_0 = -\frac{4.364}{1+\nu}$. This result is consistent with the value of $\bar{\epsilon}_0 = -\frac{4.363}{1+\nu}$ estimated by Ziebart in [20]. In Table 1, the residual strain for second bifurcation ($\bar{\epsilon}_0^{c_2}$) is given for different values of the Poisson ratio. Our results are in good agreement with those obtained by finite elements method, see [20], page 103. Note, however, the large difference in the degree of freedom.

5.2. Experimental validation

Here we show the applicability of the aforementioned buckling model to a practical situation, i.e. the manufacturing of free-standing high-temperature fuel cell membranes. We also examine the correct implementation of the numerical method.

In the context of micro solid oxide fuel cell (μSOFC) development, an yttria-stabilized zirconia (YSZ) electrolyte film of 300 nm thickness and 390 μm side length was prepared by pulsed laser deposition (PLD) at a temperature of 700 °C [10] on a free-standing silicon nitride layer fixed on a rigid etched silicon substrate, see Fig. 6. Clearly the stability of such SOFC membrane must be guaranteed in all fabrication steps. After cooling down high compressive residual stresses arise in the YSZ deposited film and buckling takes place. These residual stresses were estimated from wafer curvature analysis based on the optical measurements and by application of the Stoney formula [23]. It turned out that the effective value of the compressive residual stress in the free standing YSZ membrane is $\sigma^0 = -275$ MPa. Furthermore, the Young modulus of the YSZ film of $E = 200$ GPa was obtained by using a nanoindentation test and the Poisson ratio was estimated as $\nu = 0.25$.

5.2.1. Simulation results compared to optical profilometry measurement

The deformation of the buckled YSZ pattern was measured at room temperature by applying an optical profilometry technique using a Wyko NT100 white light interferometer. The buckling shape and amplitude was detected with high accuracy and is shown in Fig. 7(a). Note that the secondary buckling mode is clearly visible.

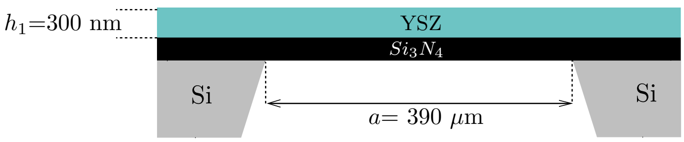

Fig. 6. A YSZ membrane is deposited on a silicon nitride layer fixed on a silicon substrate.

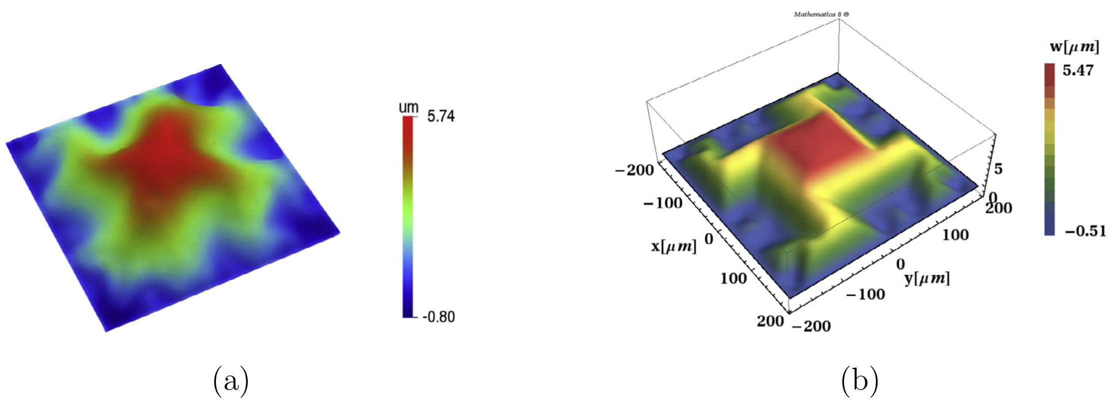

Fig. 7. (a): 3D view of an 8YSZ membrane at room temperature taken with white light interferometry of a free-standing 300 nm YSZ membrane deposited by PLD at 700 °C. (b): Simulation results using an in-house *Mathematica* code.

On the other hand, numerical simulations were performed choosing a high order degree of the Rayleigh–Ritz expansion with $m = 10$ and $p = 20$. This corresponds to $2p^2 + m^2 = 900$ unknowns. The use of in-plane equilibrium conditions, Eq. (25), reduces the degree of freedom of the problem to $m^2 = 400$. The simulation results shown in Fig. 7(b) are in agreement with the experimental buckling pattern shown in Fig. 7(a). The obtained amplitudes are comparable to the measured values with 5% of difference relatively to the maximum amplitude. This slight deviation is associated with inelastic energy dissipations [24]. Furthermore, the diagonal folds in the buckled film exhibit more slight deviation from the rotational symmetry compared to some other samples (see, e.g., the sample shown in Fig. 1 where the image is obtained using light microscopy). This is associated to some uncontrollable imperfection conditions that emerged during the fabrication. The buckling model of a compressed film exposed to load and geometry imperfections is currently our ongoing study using an energy perturbation approach (to appear in a new publication).

5.3. Energy-interpretation of buckling shape

We performed numerical simulation tests on thin films with selected values of side lengths. The obtained results are shown in Fig. 8. They exhibit typical shapes of membrane configuration corresponding to different states of mechanical equilibria.

In the pre-buckling stage, Fig. 8(a), the assumed magnitude of the residual stress of $\sigma_0 = -4.50$ MPa is smaller than that of the buckling load of $\sigma_0^{c_1} = -6.17$ MPa; the film therefore is flat. In this state, the pre-buckling potential energy is stored exclusively as membrane contraction energy. This is because the film is clamped at the boundaries and under compression with respect to the reference configuration of the stress-free shape. The potential energy in the pre-buckling stage is "strongly increasing" as the in-plane residual compression is augmented.

Furthermore, the post-buckling stage under a high residual stress $\sigma_0 = -275$ MPa is shown in Fig. 8(b). The buckling permits for a "lower increase" of the total potential energy by a transfer from membrane to bending energy. Note that the membrane-shear energy storage is minor in the first buckling stage and this in fact justifies the axis-symmetry shape of the buckled film.

The transition to the secondary buckling is shown in Fig. 8(c) for a film thickness of $h = 157$ nm. This stage is characterized by the symmetry breaking associated with a new mode of energy storage: a certain amount of membrane energy is released by elongation deformation, another amount is transferred to bending energy and a considerable amount of the membrane energy is stored as membrane shear energy. This can only be ensured by breaking the mirror symmetry of the deformation. Finally, the remaining membrane energy is still stored as membrane contraction.

The deformations in Fig. 8(d)–(f) represent an advanced stage of secondary buckling under $\sigma_0 = -275$ MPa and for side lengths of $a = 390$, 600 and 700 nm, respectively. To go from the flat shape towards this buckling shape the thin film needs to release a higher amount of the membrane energy by more elongation and needs to transfer a higher amount of the membrane energy to bending energy. The film of thickness h has a bending stiffness of order h^3 which is very low compared to the elastic membrane stiffness of order h, see Eqs. (9)–(11). Hence, to absorb the transferred energy as bending potential energy, the thin film should deform more, i.e. it should have more local curvature. This explains the observed branched and wrinkling folds at the boundaries.

Note also that the folds in Fig. 8(f) are more twisted compared to those shown in Fig. 8(c). and this is explained by a higher amount of membrane contraction energy transferred to membrane shear energy.

5.3.1. Side note on the Fig. 8(a) and (b):

In principle, the unbuckled state of the elastic material is reproducible. Indeed, when the object is relaxed without viscous, friction or damage dissipations, the potential energy is transformed into kinetic energy and the system restores its original pre-buckling configuration, see Fig. 8(a) and (b). Note however that this "reproducibility" does not necessarily imply a thermodynamic reversible process unless one assumes the buckling transition to be a sequence of equilibrium states between the pre-buckling and post-buckling stages. This assumption is realistic when buckling is not regarded as a jump transition like for example when geometrical imperfections (i.e. initial deviations from perfect plate configuration) are considered. Indeed, if the thin film undergoes an initial bending related to the manufacturing conditions the deformation will start far below the theoretical buckling load [25,26] and buckling amplitude increases gradually (as a sequence of stable configurations) when applied load increases.

5.4. Load-geometry conditions for stress relaxation in post-buckling regime

Fig. 9 shows three different buckling test cases under the same value of residual compressive stress of $\sigma_0 = -275$ MPa. It is observed that a thin film of short side length of 115 μm exhibits a primary buckling mode whereas the films of wider side lengths of 157 μm and 700 μm are in their secondary buckling mode. The film in the primary buckling mode experiences a high tensile stress in the lower surface near the boundaries, see Fig. 9, (b_1).

To identify the yielding (or failure) parts of the film, we applied Rankine criterion for safety which is based on the extremum value of the principal stresses σ_I and σ_{II}:

$$\sigma_c < \min\{\sigma_I, \sigma_{II}\}, \max\{\sigma_I, \sigma_{II}\} < \sigma_t.$$

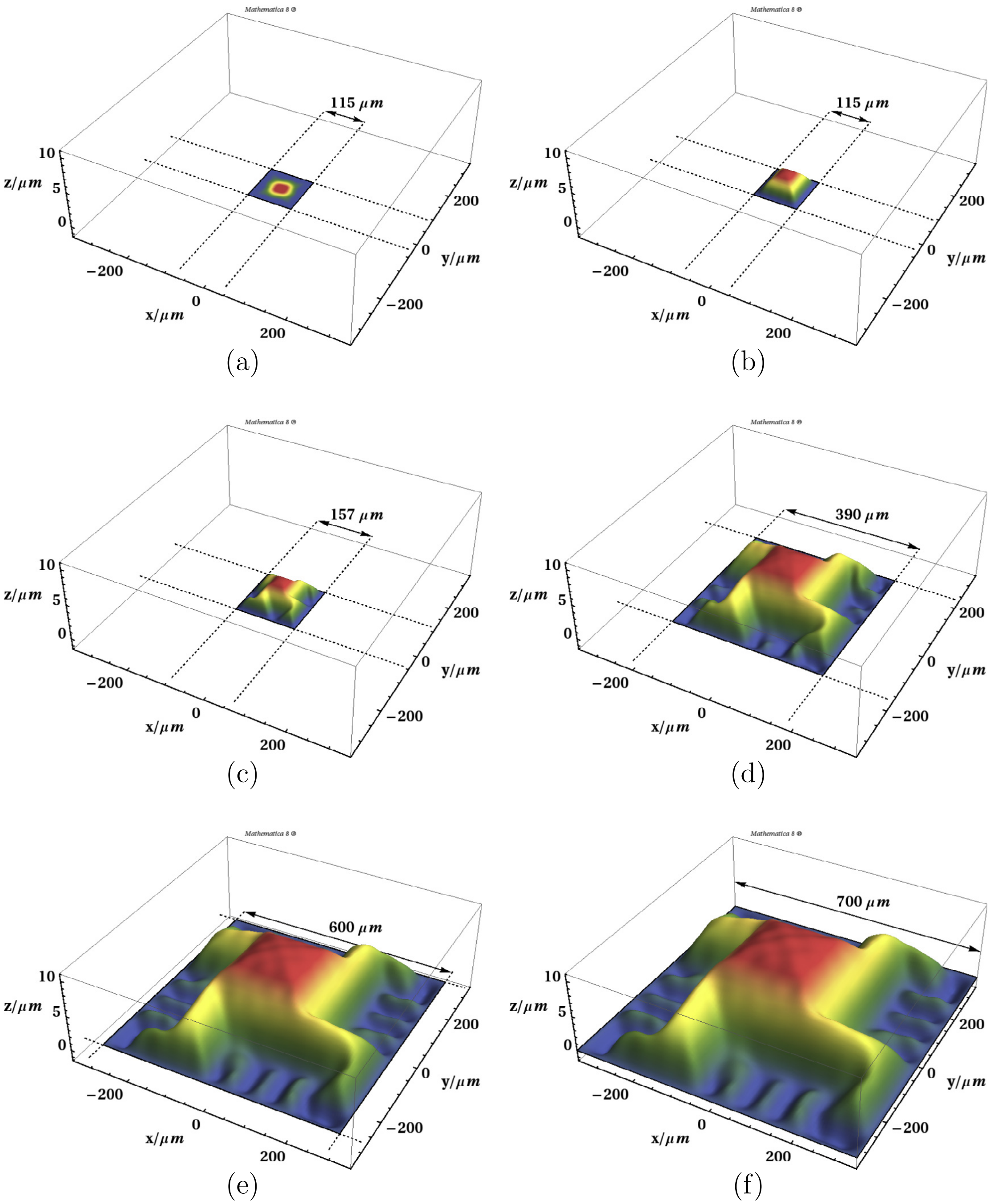

Fig. 8. Numerical results for the thin film of thickness h = 300 nm. (a): pre-buckling for $\sigma_0 = -4.25$ MPa and side length a = 115 μm. (b): primary buckling with axis symmetry for residual stress $\sigma_0 = -275$ MPa and side length a = 115 μm. (c), (d), (e) and (f): secondary buckling stages with C_4^z symmetry for $\sigma_0 = -275$ MPa and side lengths a = 157, 390, 600 and 700 μm, respectively.

When the film side length is increased to 157 μm the yielding is detected in the high tension zones in the lower surface of secondary buckling film, see Fig. 9(b$_2$) and (c$_2$). Moreover with a film of 700 μm side length we observe even more stress relaxation within an advanced stage of secondary buckling and hence the film in this example becomes almost safe.

The stress relaxation in post-buckling stage is shown in Fig. 10(a) and (b), where the extrema of the stresses are plotted against different values of the side length and the load. Rankine criterion for safety was used to determine safe lengths and safe loads. The post-buckling tensile stresses are found to be relaxed beyond the safety threshold values i.e. $a > 310$ μm for $\sigma_0 = -300$ MPa and $\sigma_0 > -220$ MPa for $a = 200$ μm. The computations have been reproduced with different values of

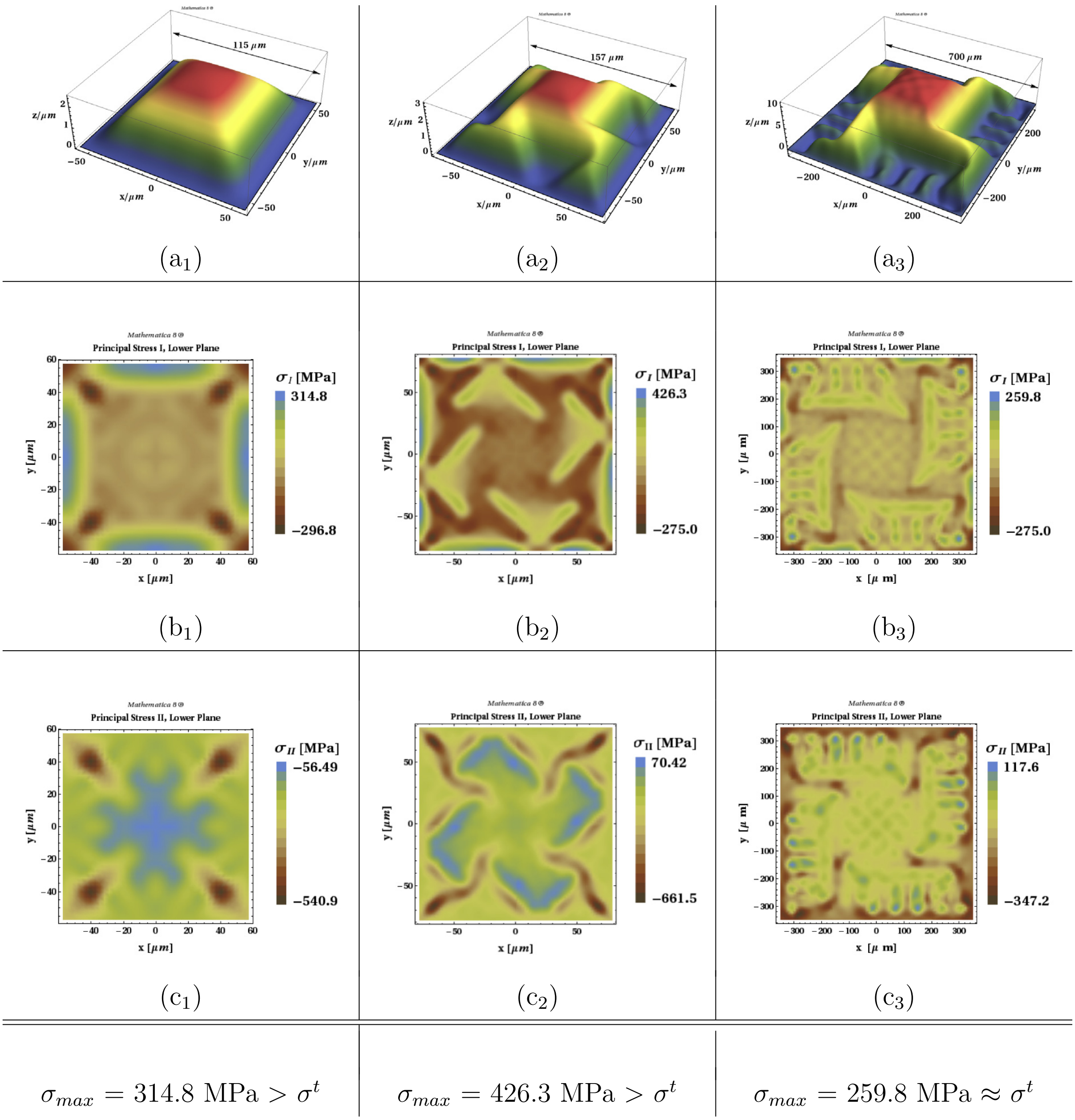

Fig. 9. Numerical results for a film of 300 nm thickness under residual compressive stress of $\sigma_0 = -275$ MPa. The simulations were performed with high degree of Ritz expansion of $m = 10$ and $p = 20$. The subscripts $i \in \{1, 2, 3\}$ stand for the three test cases with side lengths 115, 157, and 700 μm. (a_i): film shapes in primary and secondary buckling modes. (b_i) and (c_i): principal stresses σ_I and σ_{II} on the lower surface. Yielding regions are detected where the maximum stress $\sigma_{max} = \max\{\sigma_I, \sigma_{II}\}$ is above the tensile strength of $\sigma^t = 250$ MPa (Rankine criterion).

residual stresses and the least square method has been applied to represent the safety length as nonlinear function of the residual stress.

By performing the simulations for the different buckling stages a design space distinguishing between mechanically safe and unsafe conditions was obtained. This is shown in Fig. 11. Note first that the yielding regions above the tensile strength and below the compressive strength are excluded from the area of safe design. This is shown as the two horizontal lines. In between those two horizontal lines three different safe regions are found: the first is the unbuckled region which is located above the primary buckling curve. It is a region of low stress and represents the classical conservative area of buckling based failure design. The other regions are located above the limiting curves of stress relaxation in the post-buckling regime. In fact, for the micro SOFC example discussed in Section 5.2, it turns out that the safe post-buckling region is preferred over the safe pre-buckling region.

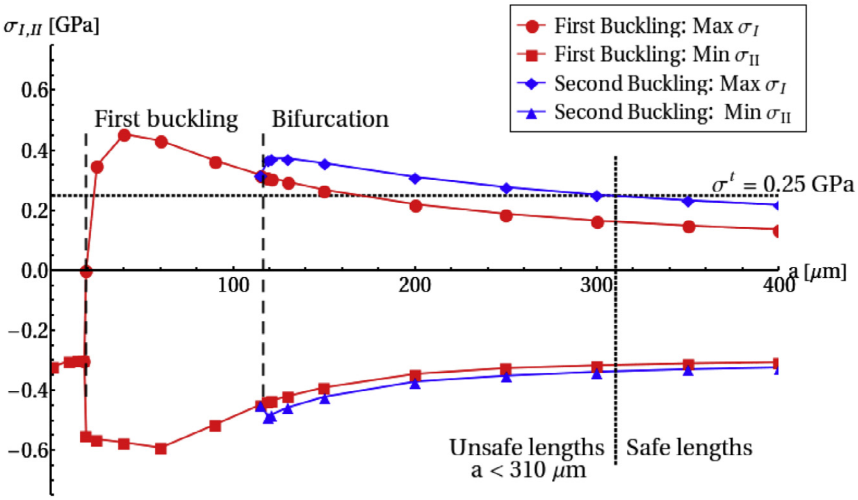

(a): σ_0= -300 MPa

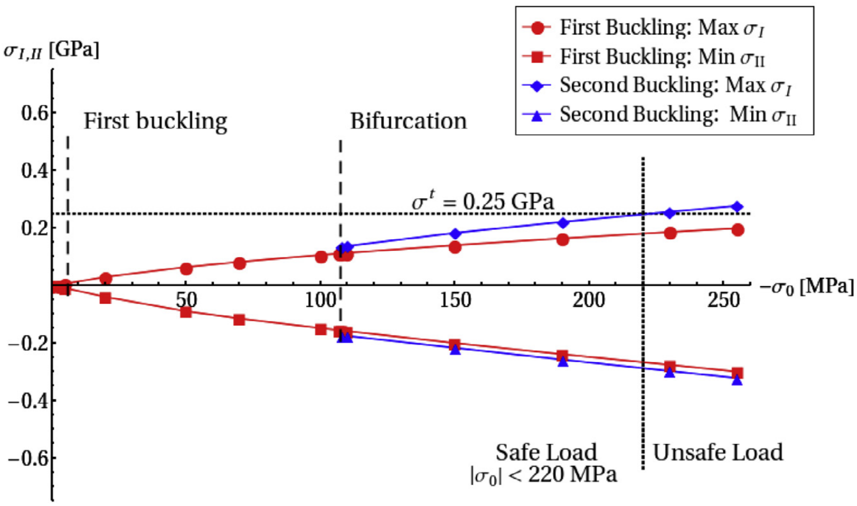

(b): a= 200 μm

Fig. 10. Extrema of principal stresses of the first and second buckling stages: (a) for residual stresses of $\sigma_0 = -300$ MPa and (b) for a side length $a = 200$ μm (b). Films of thickness of $h = 300$ nm thickness are considered with a tensile strength of $\sigma^t = 250$ MPa. The simulations are performed with a degree of Ritz expansion of $m = 3$ and $p = 6$.

Although the shown stress analysis is performed with Rayleigh–Ritz degrees of $m = 3$ and $p = 6$, the analysis of high order buckling modes, is expected to yield similar assessment of the post-buckling safety for the given residual compressive stress with restricted value of side length to thickness ratio.

Indeed, the post-buckling failure of the film is associated with the uncontrolled tensile stresses arising in the folds of the buckled pattern due to the bending effects. We consider the case of side length to thickness ratio $a/h < 1300$ restricted in the range of our experimental validation tests on safe and cracked films as shown in Fig. 11. We discuss the effects of bending stress related to the onset of the "small" buckles near the boundary of the film. This takes place with a smallest buckling wavelength λ that can be related to the film thickness through $\lambda = O(h^{\alpha})0 < \alpha < 1$, see [27], Chapter 4, [28,29]. For a given residual compressive stress, the post-buckling bending stress is given by $\sigma^b = -\frac{E}{1-\nu}\frac{h}{2R}$ where R denotes the curvature radius directly proportional to λ, hence it is depending on the thickness with the same order i.e. $R = O(h^{\alpha})$. Therefore, the related tensile bending stress depends on the thickness through $\sigma^b = O(h^{\beta})$ where $0 < \beta = 1 - \alpha < 1$, implying that, for a given

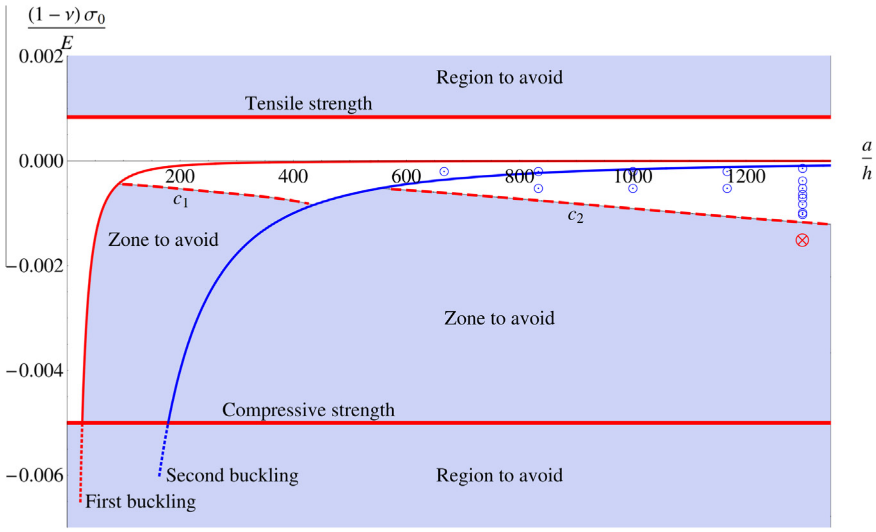

Fig. 11. An example of design space for the fabrication of a thin YSZ film with $E = 240$ GPa, $\nu = 0.2$, a tensile strength of $\sigma^t = 250$ MPa and compressive strength of $\sigma^c = -1500$ MPa. Under residual compression, the pre-buckling state occupies only a narrow region of negative residual strain above the curve of the first buckling. The first and the second post-buckling regions (below the first and the second buckling curves) include high tensile stress zones to be avoided. They are located below the dashed curves c_1 and c_2. The post-buckling regions include also large safe zones located above curves c_1 and c_2. Therefore, post-buckling design allows a wide range of options for a safe selection of deposition conditions (residual stresses) and membrane dimensions. The simulations were performed with the expansion degree of $m = 3$ and $p = 6$. Experimentally, all the 8YSZ samples produced by pulsed laser deposition (PLD) at different temperature under 20 mTorr pressure have survived the deposition and were found in the predicted safe region marked as $\odot$. The 8YSZ samples deposited at 400 °C under 2 mTorr pressure were all cracked and found in the predicted unsafe region marked as $\otimes$.

residual compressive stress, the post-buckling bending stress decreases with a decreased film thickness. On the other hand, for a given compressive stress, increasing the side length (a) allows to reduce the curvature radius with the order of $R = O(a^{\beta})$, where $0 < \beta = 1 - \alpha < 1$, implying that post-buckling bending stress σ^b is decreased with the order of $\sigma^b = O(a^{-\beta})$. To conclude, within the aforementioned geometrical range, increasing the side length to the thickness ratio $\frac{a}{h}$, is beneficial in reducing the post-buckling tensile stress and in sustaining the residual compressive stress by buckling.

It should be pointed out that our experimental tests have shown a high survival rate of square 8YSZ films in postbuckling regime especially when PLD deposition was performed at different temperature under 20 mTorr. All the samples that have survived the deposition were found in the predicted safe region of the derived design space shown in Fig. 11 where the corresponding points $(\frac{a}{h}, \sigma_0)$ are marked as $\odot$. Moreover, the 8YSZ samples deposited at 400 °C under 2 mTorr pressure were all cracked and actually found in the predicted unsafe region and marked as $\otimes$.

6. Conclusions

The presented buckling model is solved using the Rayleigh–Ritz parameterization. As demonstrated, the energy method is an efficient numerical tool for the study of the buckling phenomena. In particular, it provides boundaries for the safe manufacturing of free-standing thin films under both pre- and post-buckling conditions. The model-based analysis of the underlying physics allows one to significantly reduce the experimental effort necessary to explore safe manufacturing and operation conditions, see e.g. [30,31] (p. 40). Furthermore, the incorporation of inelastic effects into the model allowed for a high-fidelity nonlinear analysis with a more consistent representation of the energy storage. A possible extension would be the inclusion of loading and geometrical imperfections by the feature of energy perturbation approach.

Another improvement would be a new formulation of Rayleigh–Ritz approach that allows one to apply the analysis with different plate geometries and different boundary conditions. This is can be done by applying a mapping from the square domain to the reference domain and then transform the integration to the square geometry where energy minimization problem should be solved. Another way to apply the model on different geometries is to multiply the trial functions by a suitable second order smooth cut-off function with a support equal to the film domain. This would also be a topic of a following paper.

Acknowledgements

The authors are grateful for the fruitful collaboration with A. Evans, M. Prestat, M.V.F. Schlupp, R. Tölke and A. Bieberle from the Nonmetallic and Inorganic Materials group of L.J. Gauckler at the Swiss Federal Institute of Technology Zurich

(ETHZ). D. Courty from the Nanometallurgy Laboratory at ETHZ is thanked for providing the nanoindentation measurements. The authors also would like to thank A. Neels and O. Sereda from the Centre Suisse d'Électronique et de Microtechnique (CSEM), Neuchâtel, for discussing stresses in thin films. D. Briand and J. Courbat from the group of N.F. de Rooji at SAMLAB Laboratory at École Polytechnique Fédérale de Lausanne (EPFL) are also acknowledged for providing the optical profilometry measurements and discussing. The authors gratefully acknowledge the comments of the anonymous referees. Finally, the authors wish to thank the Swiss National Foundation for financial support under SNF, Sinergia contract # CRSI22-126830.

References

[1] G.Y. Grondin, A.E. Elwi, J.R. Cheng, Buckling of stiffened steel plates-a parametric study, J. Construc. Steel Res. 50 (1999) 151–175.
[2] N. Yamamoto, D.J. Quinn, N. Wicks, J.L. Hertz, J. Cui, H.L. Tuller, B.L. Wardle, Nonlinear thermomechanical design of microfabricated thin plate devices in the post-buckling regime, J. Micromech. Microeng. 20 (2010). 035027 (9pp).
[3] C. Chen, W. Tao, Z.J. Liu, Y.W. Zhang, J. Song, Controlled buckling of thin film on elastomeric substrate in large deformation, Theor. Appl. Mech. Lett. 1 (2011) 021001.
[4] H. Jiang, Y. Sun, J.A. Rogers, Y. Huang, Post-buckling analysis for the precisely controlled buckling of thin film encapsulated by elastomeric substrates, Int. J. Solids Struct. 45 (2008) 2014–2023.
[5] H. Jiang, Y. Sun, J.A. Rogers, Y. Huang, Mechanics of precisely controlled thin film buckling on elastomeric substrate, Appl. Phys. Lett. 90 (2007) 133119-1–133119-3.
[6] S. Paspuleti, Mechanical and Thermal Buckling of Thin Films Master Thesis, University of Missouri-Columbia, 2005.
[7] M. Nastasi, Intrinsic Stress in Ion Synthesized Materials (Thin Films) NATO-ASI Radiation Effects in Solids. Erice, Sicily, Italy, 17–29 July, 2004.
[8] A. Misra, M. Nastasi, Evolution of tensile residual stress in thin metal films during energetic particle deposition, J. Mater. Res. 14 (12) (1999).
[9] Y. Kuru, S.R. Bishop, J.J. Kim, B. Yildiz, H.L. Tuller, Chemomechanical properties and micro-structural stability of nanocrystalline Pr-doped ceria: an in situ X-ray diffraction investigation, Solid State Ionics 193 (2011), http://dx.doi.org/10.1016/j.ssi.2011.04.012.
[10] A. Evans, Residual stress and buckling patterns of free-standing yttria-stabilized-zirconia membranes fabricated by pulsed laser deposition, Fuel Cells 12 (4) (2012) 614–623.
[11] G. Gioia, A. DeSimone, M. Ortiz, A.M. Cuitiño, Folding energetics in thin-lm diaphragms, Proc. R. Soc. Lond. A 458 (2002) 1223–1229.
[12] K. Kerman, T. Tallinen, S. Ramanathan, L. Mahadevan, J. Power Sources 222 (2012) 359–366.
[13] T. Tallinen, J. Ojajãrvi, J.A. Åström, J. Timonen, Scaling behavior in non-Hookean compression of thin-walled structures, Phys. Rev. Lett. 105 (2010) 066102.
[14] M. Ortiz, Delamination of Compressed Thin Films Workshop on Material Interfaces and Geometrically Based Motions IPAM/UCLA, April 26, 2001.
[16] O.A. Bauchau, J.I. Craig, Structural Analysis, Solid Mechanics and Its Applications, Volume 163 Series Editor Gladwell G M L, 2009.
[17] A.W. Leissa, The historical bases of the Rayleigh and Ritz methods, J. Sound Vib. 287 (2005) 961–978.
[18] R.M. Jones, Buckling of Bares, Plates and Shells, Bull Ridge Publishing, 2006.
[19] L. Bauer, H.B. Keller, E.L. Reiss, Multiple eigenvalues lead to secondary bifurcation, SIAM Rev. 17 (1) (1975) 101–122.
[20] V. Ziebart, Mechanical Properties of CMOS Thin Films (PhD thesis), Swiss Federal Institute of Technology ETH Zurich, 1999.
[23] G.G. Stoney, The tension of metallic films deposited by electrolysis, Proc. R. Soc. London Ser. A 82 (1909) 172.
[24] C. Hollauer, Modeling of Thermal Oxidation and Stress Effects (PhD Thesis), Technischen Universität Wien, Austria, 2007.
[25] A.W. Leissa, Buckling and post-buckling of composite plates 3–32, G.J. Turvey, I.H. Marshall (Eds.),1995.
[26] A.W. Prabu, Investigation on the effects of general initial imperfections on the buckling of thin cylindrical shells under uniform axial compression (PhD Thesis), Principal, Rajiv Gandhi College of Engineering and Technology, Pondicherry, India, 2007.
[27] Y. Ebatta, Bending, Wrinkling, and Folding of Thin Polymer Film/Elastomer Interfaces (PhD thesis), University of Massachusetts, 2013.
[28] E. Cerda, T. Mahadevan, Geometry and physics of wrinkling, Phys. Rev. Lett. 90 (7) (2003).
[29] J.S. Sharp, K.R. Thomas, M.P. Weir, Mechanically driven wrinkling instability in thin film polymer bilayers, Phys. Rev. E 75 (2007) 011601.
[30] J.H. Starnes, Hildbuger, Jr., M.W. Hildbuger, Using High-Fidelity Analysis and Experimental Results To Account for the Effects of Imperfections on the Buckling Response of Composite Shell Structures RTO AVT Symposium Paris France, 2002.
[31] B.G. Falzon, M.H. Aliabadi (Eds.), Computational and Experimental Methods in Structures, Buckling and Post-Buckling Structure, Experimental, Analytical and Numerical Studies, Vol. 1, Imperial College Press, 2008.

Further reading

[15] Y. Tang, K. Stanley, J. Wu, D. Ghosh, J. Zhang, J. Micromech. Microeng. 15 (2005) 185–192.
[21] D. Coffin, F. Bloom, Handbook of Thin Plate Buckling and Post-buckling (Hardcover), 2001.
[22] F.N. Herman, Mechanics of interface fracture with applications in electronic packaging, IEEE Trans. Device Mater. Reliab. 3 (4) (2003).